

Microstructure and mechanical properties of magnesium alloy AZ31B laser beam welds

R.S. Coelho^a, A. Kostka^{a,*}, H. Pinto^a, S. Riekehr^b,
M. Koçak^b, A.R. Pyzalla^a

^a Max-Planck-Institut für Eisenforschung GmbH, 40237 Düsseldorf, Germany

^b GKSS Research Center GmbH, 21502 Geesthacht, Germany

Received 9 March 2007; received in revised form 17 July 2007; accepted 20 July 2007

Abstract

Microstructure and properties of a Mg AZ31B laser beam weld without filler are studied using electron microscopy, X-ray diffraction and mechanical tests. The microstructure of the weld is characterized by a narrow heat affected zone, columnar grains and precipitate coarsening in the fusion zone. Texture in the fusion zone is significantly different from the texture of the base material. The residual stress distribution observed is similar at the top and the bottom of the weld, maximum tensile residual stress values are observed in the fusion zone. Tensile tests reveal differences in the mechanical behavior of the fusion zone and the parent material, which can be related to the differences of texture and the resulting deformation mechanisms.

© 2007 Published by Elsevier B.V.

Keywords: Magnesium; Microstructure; Texture; Laser welding; Mechanical properties

1. Introduction

Because of their extremely low weight in combination with their good castability, workability and damping capacity [1], the use of magnesium and its alloys in specific structural applications increases, often replacing aluminium alloys [2,3]. In order to further widen the field of application of Mg alloys, joining processes such as tungsten inert gas welding (TIG), laser beam welding (LBW), friction stir welding (FSW) and electron beam welding have been applied to weld magnesium alloys [4–7]. Among these processes LBW is particularly attractive for innovative and cost-effective applications, which require high precision, and processing speed [8,9].

Although heat input in laser welding is rather low, temperature cycles, and thus recovery and recrystallization in the melt pool and heat affected zone (HAZ) produces significant microstructure changes. These changes include local variations of grain size, precipitate size, shape, distribution and orientation and, thus, have a strong influence on mechanical properties.

The mechanical properties of the welded joint are determined by the properties of the joint constituents (basically parent material, HAZ and fusion zone). Further, residual stresses, due to their superposition with applied stresses may have a crucial influence primarily on the fatigue strength of welds.

In Mg-alloy welds microstructure–property relations are of particular interest. The ductility of commercially used Mg alloys, due to their hexagonal close packed (hcp) crystal lattice, is limited by the number of slip systems on both basal and non-basal planes, which are activated during deformation [10–13]. In addition to dislocation slip also twinning contributes to plastic deformation of Mg alloys. Whereas the microstructure–property relations of Mg alloy sheet material have been studied intensively [1,14–17], knowledge about microstructure–property relations of welds so far is scarce. The deformation mechanisms activated during deformation of a weld depend strongly on the microstructure and texture of the fusion zone, the HAZ and the base material and the residual stress state of the welds.

It is interesting to compare the microstructure–property relations of laser beam welded joints with these obtained in friction stir welding process, where metallic bond is achieved below the melting point of the base material and, thus, avoiding diverse problems associated with the solidification process. Friction stir welded joints of magnesium alloys have received a lot of

* Corresponding author. Tel.: +49 211 6792989.

E-mail address: a.kostka@mpie.de (A. Kostka).

interest in science and technology, and so recently have been intensively studied [18–24]. A number of investigations have shown that under the influence of the FSW tool (i.e. mechanical deformation) and processing temperatures a fine recrystallized microstructure is formed in the stir zone [25]. These fine recrystallized grains in the stir zone improve the local properties of this region. It is also reported that the high dislocation density in the weld region further contributes to a more homogeneous hardness profile for FSW Mg alloys [7]. Likewise to the LBW, the integrity and performance of FSW joints of magnesium alloys can be significantly influenced by changes in the texture during the friction stir welding process. Recently, Park et al. studied the fractured surface of a FSW AZ61 Mg alloy tensile specimen and observed a strong texture (i.e., basal plane was tilted 45° from the fracture surface normal) [25]. Other examples include: micro-texture evolutions in AZ61 [26], tensile properties of AZ31B-H24 [27], and grain size/orientation of AZ31 [28] after FSW. However, the relation between the microstructure and the mechanical properties of the FSW as well as LBW has not been fully established.

Therefore, this study is conducted to investigate and establish the relationship between microstructure and mechanical properties of the laser beam welded Mg-alloy AZ31B. In particular, the effect of the different crystallographic textures in fusion zone, HAZ and base material on the plastic deformation behavior of AZ31B LBW is investigated systematically.

2. Experimental details

2.1. Material

AZ31B magnesium alloy rolled plates in original dimensions of 2 mm \times 1300 mm \times 1000 mm size with a nominal composition of 3.34–3.63 wt% Al, 0.45–0.53 wt% Zn, 0.27–0.29 wt% Mn, balance Mg were purchased at Sinomag company, China.

2.2. Laser beam welding

Nd:YAG Laser Beam Welding was used to join 2 mm thick rolled magnesium alloy AZ31B at the GKSS Research Center Geesthacht, Germany. Butt welds were manufactured by joining plates of 200 mm \times 330 mm \times 2 mm (Fig. 1) without wire on a vacuum clamping table. The welding parameters chosen were: 2.2 kW laser power, 5.5 m/min welding speed, 0 mm focal point, helium shielding gas (16 l/min on the top side and 40.7 l/min on the bottom side), no post-welding heat treatment was performed. The welding direction (WD) coincides with the rolling direction (RD) of the Mg-alloy sheets.

2.3. Mechanical tests

Standard flat tensile test specimens with gauge sections of 2 mm \times 12 mm \times 70 mm were extracted by spark erosion cutting from the base material and the welds both in welding direction (WD) and in transversal direction (TD) of the specimens (Fig. 1). Additional tensile tests of the welded joints in TD were performed up to different deformation levels to clar-

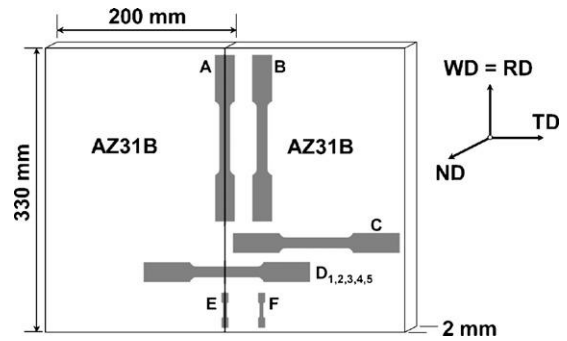


Fig. 1. Schematic overview of the configuration of the AZ31B magnesium alloy plates joined by laser beam welding in but-joint without wire. The configuration of the machined tensile samples of the welded joint and the base material is shown. WD, welding direction; TD, transversal direction; ND, normal direction.

ify the active deformation micromechanisms; specimens were deformed up to different deformation levels of 0.35% (sample marked as D₁), 0.59% (sample marked as D₂), 0.9% (sample marked as D₃) and 4.5% strains (sample marked as D₄), respectively.

In order to determine the mechanical properties of the fusion zone, micro-flat tensile (MFT) test samples with a gauge length of 9 mm, 1.5 mm width and 0.5 mm thickness were manufactured from the material in the fusion zone. The longitudinal direction of these MFT samples coincides with the welding direction (WD). This test technique has been specially developed at the GKSS to be able to determine the stress strain curves of narrow weld seams or regions with microstructural gradients (e.g. HAZ) [29]. Microhardness measurements were performed across the weld cross-section according to ASTM E384-99 standard at three different levels in plate thickness.

2.4. Metallography and microscopy

Microstructure characterization was carried out by optical microscopy, scanning (SEM) and transmission electron microscopy (TEM).

The specimens were sectioned, ground, polished using lubricant without water and etched using acetic–picric solution (10 ml acetic acid + 4.2g picric acid + 10 ml H₂O + 70 ml ethanol). For SEM investigations, after polishing, surface oxides on the specimens were removed in a Gatan Precision Etching Coating System (Gatan 862).

EBSD texture analyses were performed using a SEM with Shottky field-emission gun and an EDAX/TSL electron back scattering diffraction (EBSD) system equipped with a Digit view camera. The EBSD measurements in the fusion zone and the base material covered sample areas of 1500 μ m \times 350 μ m. Several pole figures and inverse pole figures were generated from each grain map determined.

For transmission electron microscopy (TEM) samples were first mechanically ground to a thickness of 300 μ m, then 3 mm diameter discs were blanked of the base material and fusion zone (disc out-of-plane direction is perpendicular to the normal direction (ND) of the AZ31B sheets). Mechan-

ical thinning of the disc was continued until it reached a thickness of 100 μm . Foils were obtained by electrochemical double-jet thinning using a (900 ml methanol + 180 ml 2-butoxy-ethanol + 9.5 g licyl + 20.1 g $\text{Mg}(\text{ClO}_4)_2$) electrolyte at a temperature of 243 K. In the final step of sample preparation the foils were subjected to short ion milling (Gatan Precision Ion Polishing System 691) in order to remove the surface oxide layer.

2.5. Residual stress analyses

Residual stress (RS) analysis was carried out by synchrotron X-ray diffraction at the experimental station G3 at DORIS III at HASYLAB at DESY, Hamburg, using the $\sin^2 \psi$ technique [30,31]. The radiation energy used was 6.9 keV and the beam size was 1.5 mm \times 1.5 mm. The measurements were carried out within a $\sin^2 \psi$ range of 0–0.8, step size 0.2 in $\sin^2 \psi$, using the Mg(1 1 2) reflection. Residual stresses were determined on the top and bottom side of the joint (± 30 mm from the weld centreline) both in TD and WD. In order to eliminate surface effects, additional residual stress analyses were performed in a depth of about 50 μm below the top side of the weld.

3. Results

A macroscopic view on the AZ31B LBW welds reveals a fine homogeneously structured (Fig. 2a) fusion zone of about 1 mm width. A closer view on the weld cross-section using OM shows that the fusion zone does not contain any visible cracks, but, that it contains some small pores (Fig. 2b). The maximum pore diameter observed in the fusion zone is about 50 μm .

3.1. Mechanical properties

3.1.1. Microhardness

Microhardness measurements on the cross-section of AZ31B LB welds reveal an average microhardness of about 53HV0.1 in the AZ31B sheet base material (Fig. 3). The HAZ and the fusion zone show a tendency towards slightly higher microhardness values (about 57HV0.1) compared to the base material. The microhardness profiles determined in different distances to the weld top surface were not significantly different from each other.

3.1.2. Yield strength and elongation to fracture

In order to assess the anisotropy of the mechanical properties of the welds, tensile tests were performed in rolling direction (RD) – samples A – which is identical with the welding direction (WD) and in transverse direction (TD) – samples D_n – of the welded joints (Fig. 1). Fracture of the welded joints tested in TD direction always occurred in the base material in several mm distance from the fusion line within the base material.

3.1.2.1. Standard tensile test samples. During the tensile test where loading was applied in WD, yielding of the base material occurs at 146 ± 5 MPa, whereas the yield strength of the LBW in transverse direction is measured as 148 ± 5 MPa (Table 1;

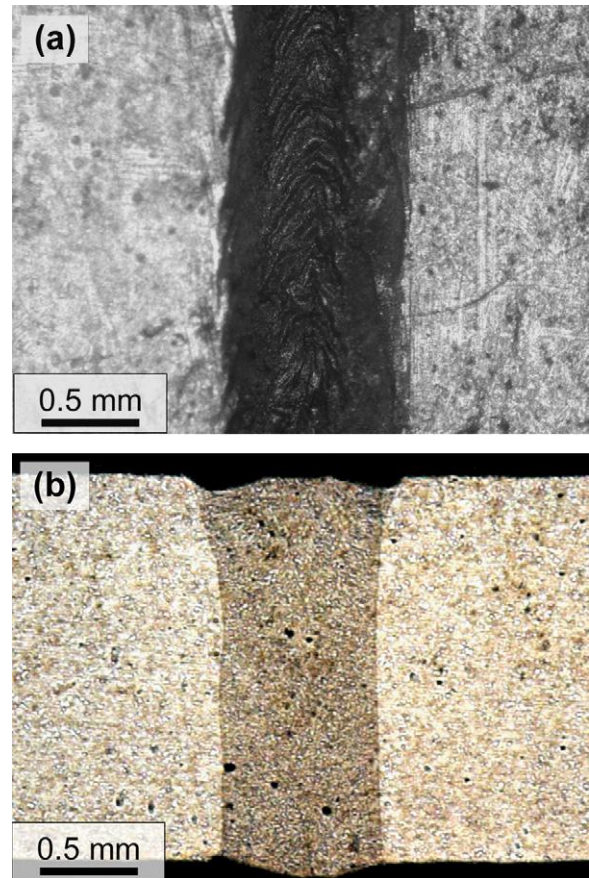


Fig. 2. Optical micrograph of the laser beam welded AZ31B magnesium alloy. Macrophoto of the weld, top view (a) and cross-section (b).

Fig. 4). Elongation to fracture in WD is about 20%, which is slightly less than in transverse direction of the Mg AZ31B sheets (24%). In contrast to the base material, samples containing a weld reach their yield strength earlier when deformed in TD (92 ± 5 MPa) compared to WD (134 ± 5 MPa). Elongation to fracture of the welded samples both in WD (about $15 \pm 1.5\%$) and TD (about $19 \pm 1.5\%$) is lower than the elonga-

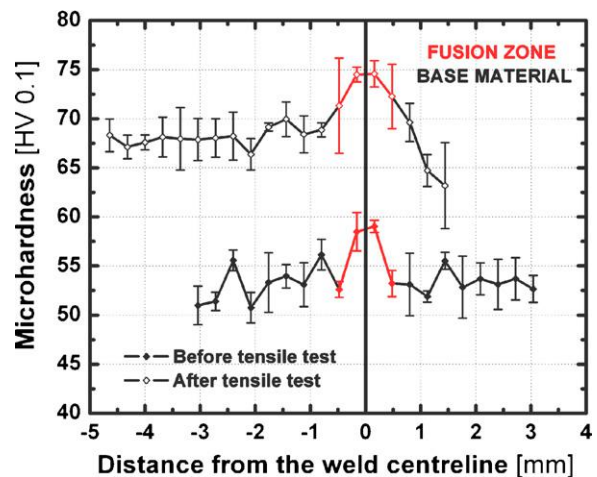


Fig. 3. Microindentation hardness profiles before (sample D_0) and after (sample D_5) tensile test show strain hardening.

Table 1
Yield, strength and strain anisotropy of the LBW AZ31B magnesium alloy in butt-joint configuration

Tensile sample	Size	WD=RD			TD		
		Rp0.2 (MPa)	Rm (MPa)	A (%)	Rp0.2 (MPa)	Rm (MPa)	A (%)
Base material							
B	Standard	146 ± 5	249 ± 5	20 ± 1.5	–	–	–
C	Standard	–	–	–	148 ± 5	251 ± 5	24 ± 1.5
F	Micro	130 ± 10	260 ± 10	20 ± 3	–	–	–
Fusion zone							
E	Micro	180 ± 10	270 ± 10	21 ± 3	–	–	–
A	Standard	134 ± 5	247 ± 5	15 ± 1.5	–	–	–
D ₁	Standard	–	–	–	–	85 ± 5	0.35
D ₂	Standard	–	–	–	–	96 ± 5	0.59
D ₃	Standard	–	–	–	–	140 ± 5	0.90
D ₄	Standard	–	–	–	–	200 ± 5	4.52
D ₅	Standard	–	–	–	92 ± 5	247 ± 5	19 ± 1.5

Sample shape, position and orientation, e.g. a–c given in Fig. 1.

tion to fracture of base material samples taken in the respective directions.

In the base material the yield stress anisotropy ratio σ_{TD}/σ_{RD} is 1.01, which is slightly lower than 1.17 given by Lou et al. [32]. The same ratio calculated for welded joint is significantly

lower ($\sigma_{TD}/\sigma_{RD} = 0.69$). Thus, LBW seems to reduce the strong mechanical anisotropy of the joints, which is caused by the strong basal texture of the cold rolled Mg sheets.

Fig. 5 shows samples after standard TD tensile test up to 0.9% (D₃) and 4.5% (D₄) strain. At 4.5% strain a strong plastic deformation of the fusion zone is observed. We note that this effect is associated with a strong texture reorientation (see Section 3.3.2).

3.1.2.2. *Micro-flat tensile (MFT) test samples.* The micro-flat tensile test samples taken in WD yields at 130 ± 10 MPa, its elongation to fracture is $20 \pm 3\%$. The yield strength of the fusion zone material, thus, is significantly higher (180 ± 10 MPa) than the yield strength of the macroscopic tensile test sample containing the weld and higher than the yield strength of the base material in WD=RD direction. The mechanical properties obtained for the base material by micro flat tensile tests in samples taken in WD agree with those of the standard tensile test sample taken from the base material in the same direction (Table 1).

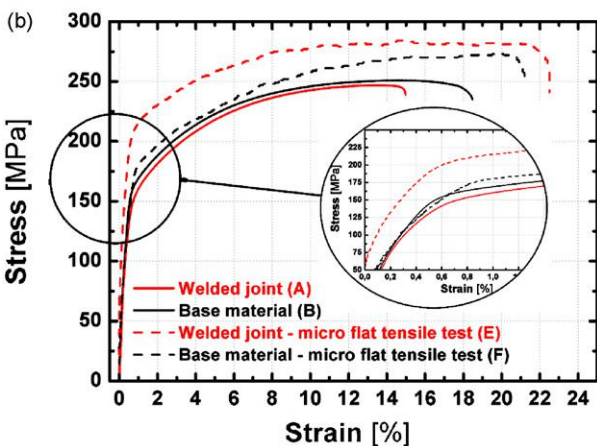
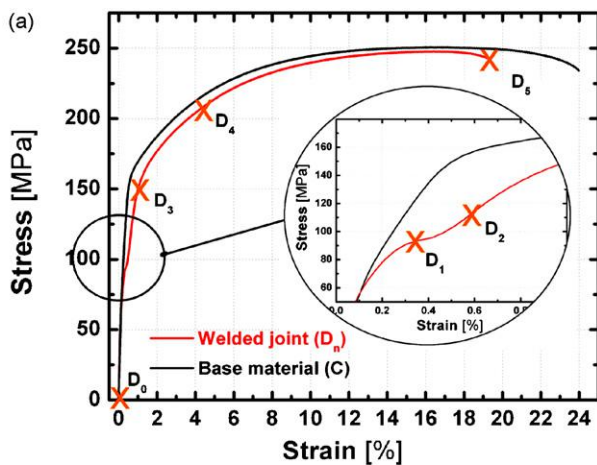


Fig. 4. Tensile stress–strain curves of the samples strained at various directions. Transversal direction (a) and longitudinal (LD=WD) direction (b).

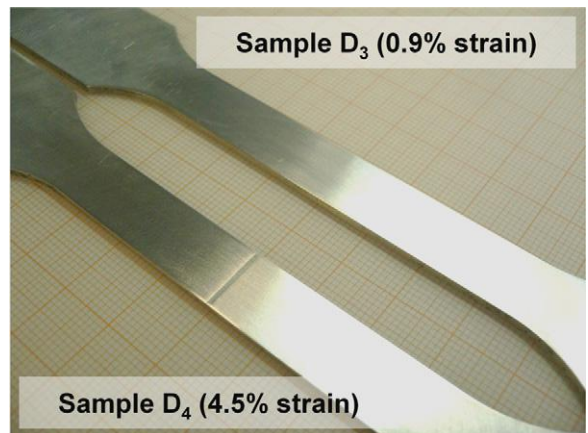


Fig. 5. Optical micrograph of the samples after TD-tensile test. Where sample D₃: 0.9% accumulated strain does not show any significant changes, sample D₄: 4.5% accumulated strain reveals significant deformation of the fusion zone.

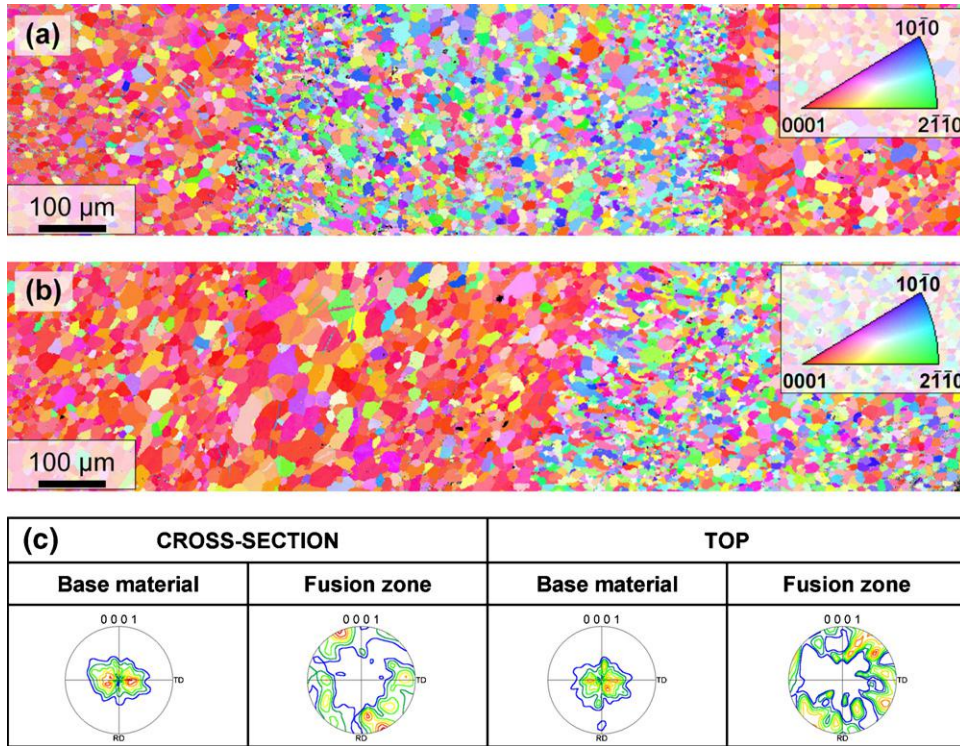


Fig. 6. EBSD inverse pole figure map of the laser beam welded AZ31B magnesium alloy prior to deformation (sample D₀). Cross-section of the weld (a) and the top view of the weld (b). Corresponding basal plane pole figures of the cross-section and top view (c).

3.2. Microstructure, texture and residual stresses

3.2.1. Weld microstructure

The AZ31B sheet base material consists of hexagonal close packed (hcp) α -Mg and β -phase $Mg_{17}(Al,Zn)_{12}$ [33] precipitates (identified by TEM diffraction patterns). The α -Mg grains are equiaxed, their average grain size is about 7.7 μm (Figs. 6 and 7). The shape of the $Mg_{17}(Al,Zn)_{12}$ precipitates is ellipsoidal, their aspect ratio determined using TEM is about 5:1, their maximum length is up to about 200 nm.

In the heat affected zone (HAZ) of the base material near the interface to the fusion zone, SEM micrographs (Fig. 8) reveal coarsening of the $Mg_{17}(Al,Zn)_{12}$ precipitates, the grain size of the α -Mg is barely affected by the heat input during welding (Fig. 7). The width of the HAZ is about 10 μm (Figs. 6 and 7).

The microstructure in the fusion zone is also characterized by α -Mg grains of slightly smaller average grain size (about 6 μm) compared to the base material. SEM-EBSD analyses revealed a gradient in grain size across the fusion zone (Figs. 6 and 7), at the interface to the HAZ grain sizes are as small as 4.9 μm , while in the centre of the fusion zone grain diameters are as large as 6.4 μm . The morphology of the grains in the fusion zone shows

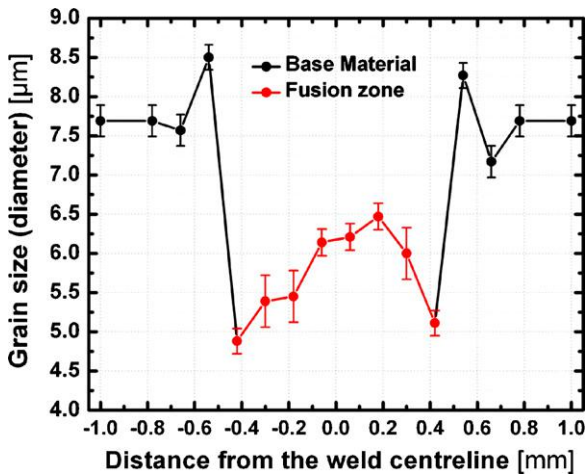


Fig. 7. Grain size distribution of the welded sample prior to the tensile deformation. Data obtained from the EBSD analyses of the microstructure shown in Fig. 3a.

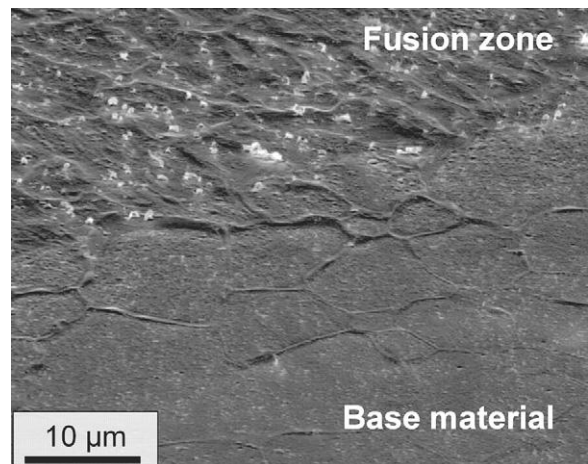


Fig. 8. SEM micrograph of the base material—fusion zone interface.

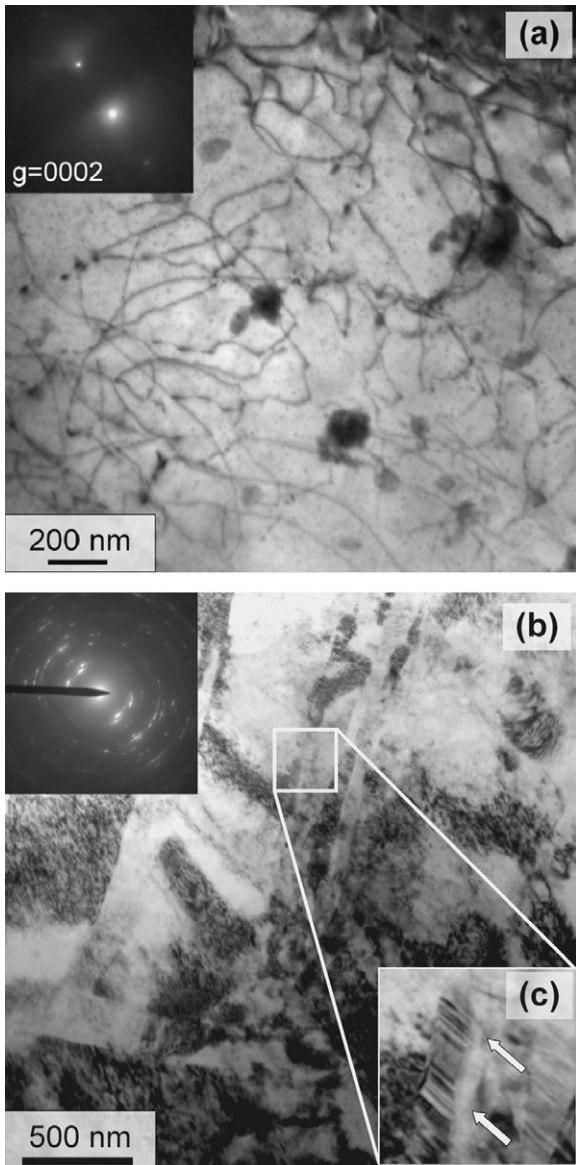


Fig. 9. TEM micrographs of the fusion zone before (sample D_0) (a) and after (sample D_5) the tensile deformation (b). Bad TEM diffraction contrast of (b) is due to an extremely high density of dislocations. Diffraction pattern corresponding to (b) represents evidence for extremely high accumulation of defects (microtwins) (c).

a transition from columnar grains near the fusion line towards equiaxed grains in the centre of the fusion zone. Dislocation and twin density in the fusion zone (Fig. 9a) are slightly higher than in the base material. The β -phase $Mg_{17}(Al,Zn)_{12}$ precipitates are significantly coarser (300–500 nm) in the fusion zone compared to the base material.

3.2.2. Texture

Fig. 10 shows pole figures obtained by EBSD for those crystallographic planes of the α -Mg, which are associated with deformation processes of the hcp structure: basal slip plane (0001), prismatic (10–10) and twinning (11–20).

In the AZ31B sheet base material (Figs. 6c and Fig. 10, sample D_0) the basal planes appear nearly parallel to the sheet normal

direction (ND), but, slightly tilted (symmetrically at an angle of about 25°) to the transversal direction.

In the fusion zone, the (0001) basal planes are tilted into welding direction (WD) ($\alpha \approx 80^\circ$) and rotated around the ND ($\beta \approx 15^\circ$) of the fusion zone.

Texture analyses performed on weld cross-sections and on top of the welds resulted in almost identical pole figures (Figs. 6c and Fig. 10, sample D_0) indicating that texture inhomogeneities in the normal direction (through-thickness) are small both in the base material and the fusion zone (see also Fig. 6, only {0001} pole figures obtained by EBSD analyses on the top side of the weld and the weld cross-section are shown for reasons of brevity).

3.2.3. Residual stresses

Residual stress (RS) distributions across the weld, which were measured at different positions across the welds, did not reveal significant differences in the magnitude of the residual stresses in longitudinal and transversal direction indicating a homogeneous residual stress distribution, where the welding process is stationary (at sufficient distance to the start and finish points).

The residual stress distribution in welding direction is symmetric with respect to the weld centreline (Fig. 11). The fusion zone contains tensile residual stresses of up to about 40 MPa in welding direction, which reach their maximum at the weld centreline and decrease with increasing distance to the weld centreline. The HAZ is under tensile stresses in welding direction, in the parent material at a distance of about 8 mm from the weld centreline the transition to compressive residual stresses occurs. At larger distances to the weld centreline the base material contains compressive residual stresses of low magnitude. In transversal direction, the magnitude of the residual stresses in general is very small (maximum compressive RS is approximately 20 MPa, maximum tensile RS is approximately 5 MPa).

The results of RS analyses performed at the bottom side and after removing a surface layer of $50 \mu\text{m}$ thickness ($z = -50 \mu\text{m}$ in Fig. 11) by electrochemical polishing do not show significant differences in RS distribution and magnitude compared to the results of the analyses of both the longitudinal and transversal RS at the top surface of the welds.

3.3. Effect of tensile deformation on weld microstructure and texture

3.3.1. Weld microstructure after tensile tests

Deformation of the samples during the tensile test results in a strong increase in twin and dislocation density (Fig. 9b and c) both in the base material and the fusion zone. TEM observations further prove the twin density to be significantly higher in the fusion zone compared to the base material.

3.3.2. Texture of the deformed specimens

After the tensile test, most crystallites in the base material keep their original orientation before plastic deformation.

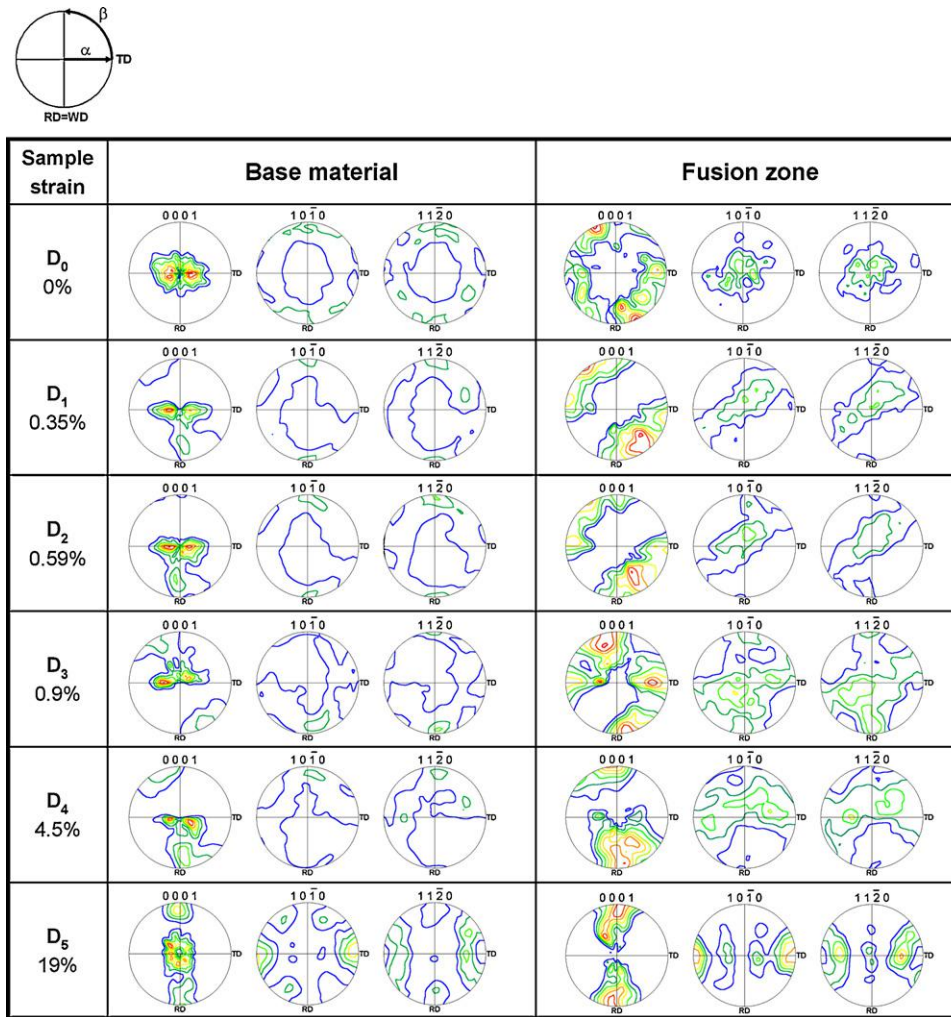


Fig. 10. Pole figures (basal $\{0001\}$ and prismatic $\{10-10\}$, $\{11-20\}$) referring the crystallographic texture at various deformation stages.

Some of the crystallites, however, reorient about 90° , thus, a second texture pole in WD appears in the (0001) pole figure of the base material after tensile deformation (Fig. 10, sample D₄). Associated with the reorientation are also texture poles in TD of the $(10-10)$ and $(11-20)$ pole figures.

Pole figures obtained in the fusion zone of the tensile deformed samples reveal a strong change in texture, the (0001) pole reorient themselves into WD. In addition, in the pole figures of the prismatic planes $(10-10)$ and $(11-20)$, poles in transversal direction appear after tensile deformation (Fig. 10, sample D₄). Pole figures shown for the intermediate stages of deformation, samples D₁ to D₃ reveal the evolution of the deformation texture. These are discussed in detail in Section 4.2.

3.3.3. Microhardness of the deformed specimens

Tensile deformation increases the microhardness both of base material and fusion zone. Strengthening (strain hardening) in the fusion zone appears to be more pronounced than in the base material (Fig. 3).

4. Discussion

4.1. Microstructure, texture and residual stress formation in LBW of AZ31B

4.1.1. Microstructure and texture of AZ31B LBW

A highly focused heat input is characteristic of laser beam welding. The heat generated is rapidly extracted from the molten fusion zone by the surrounding colder material. During the solidification process, grains therefore usually grow epitaxially from the fusion line regions of the HAZ into the fusion zone. At the fusion line where relatively large temperature gradients and a small growth rate occur, the microstructure was predominantly cellular [4].

Texture of the Mg sheet base material corresponds to the basal texture often reported for AZ31B sheet metal [32,34,35]. Texture formation in the fusion zone is driven by crystal growth, which is controlled by the vectorial heat flow direction during the solidification process [36,37]. Thus, in Mg-alloys the $\langle 11-20 \rangle$ a -axis of the hcp-crystal lattice, which is the closest-packed crystallographic direction, in crystallites within the fusion zone is

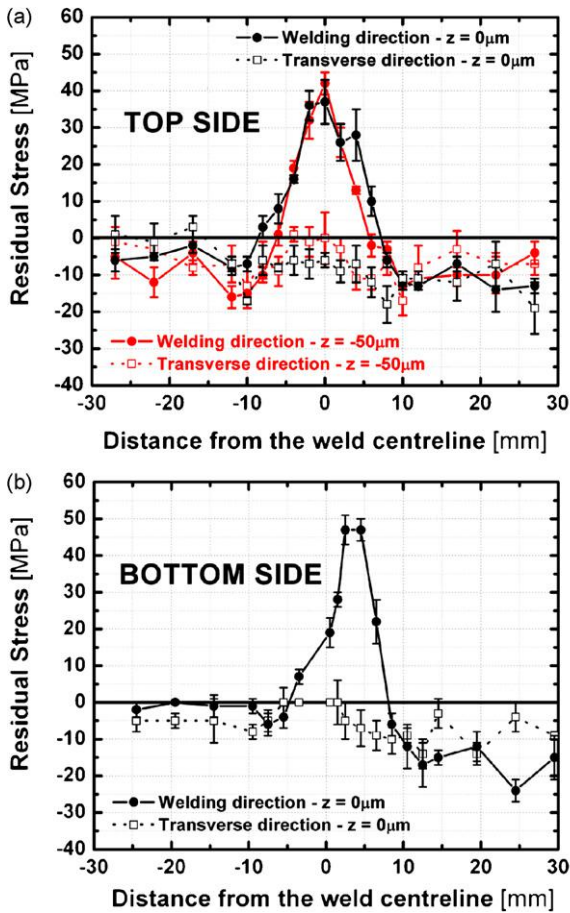


Fig. 11. Residual stress profiles of the LBW AZ31B magnesium alloy. The top side (a) and the bottom side of the weld (b).

expected to grow preferentially in heat flow direction. Due to the low depth-to-width aspect ratio of the LBW welds (maximum 2) the heat flow presumably occurs in the three main specimen directions WD, TD and ND (Fig. 12a and b). Therefore, the vector of heat flow (h_t) in the fusion zone is tilted from both WD and ND into TD. Texture in the weld is significantly different from texture in the base material, which is a near (0001) fiber texture along the ND, frequently reported for rolled Mg sheets, e.g. [32,34–36].

4.1.2. Origin and assessment of residual stresses in AZ31B LB welds

When welding a butt-joint, the high density heat input produced by the LB generates temperatures in the weld pool, which are beyond the melting point of the alloy AZ31B, while the base material remains considerably colder. Consequently, steep temperature gradients occur during heating and rapid cooling, due to preferential heat flow into the base material and the atmosphere. The inhomogeneous plastic deformation associated with shrinkage during cooling is known to result in the formation of residual stresses (RS) [38,39]. These welding residual stresses are higher for the highly stiff or constrained joint with lower distortion [40].

The similarity of the residual stress distributions determined on the top and bottom sides as well as 50 μm beneath the top surface can be attributed to the small sheet thickness of the investigated AZ31B butt-joints. The RS profiles experimentally determined in welding and transverse directions are typical for a fusion welding process. Due to the restrained thermal contraction of the weld pool during cooling in welding direction, i.e. parallel to the fusion line, the fusion zone contains tensile RS while the base material far away from the fusion zone is under

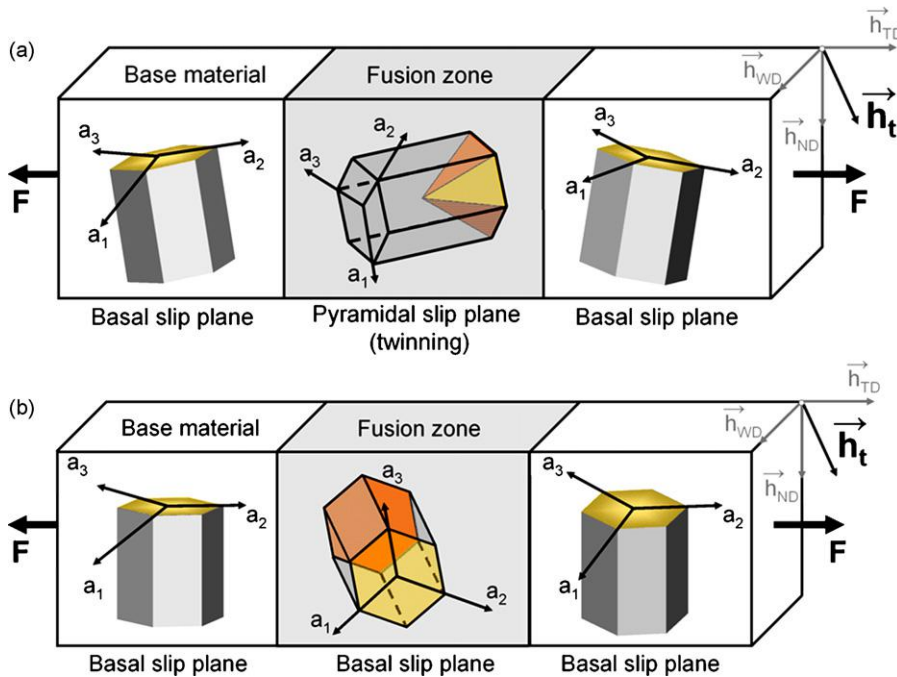


Fig. 12. Schematic overview of the crystallographic texture before (a) and after tensile deformation in transverse direction (b). The texture components of the base material and the fusion zone are presented as hexagonal unit cells with the same coordinate systems. The welding heat flow within the fusion zone during the LBW is shown in the right up corner.

balancing compressive RS. The maximum tensile RS in welding direction in the centre of the weld of about 40 MPa correspond to less than one third of the yield strength (200 MPa) [1] of the Mg-alloy AZ31B, but may, however, influence the fatigue strength of the joint [41].

4.2. Mechanical properties of AZ31B LB welds

In many structural materials, weld joints exhibit inferior mechanical properties compared to the base material. However, samples tested in WD showed comparable yield and ultimate tensile strengths to those of the base material, while the ductility of the joints is lower than those of the base material. In TD, the yield strength of the joints is significantly lower, ultimate tensile strength is similar and ductility is lower than those of the base material (Table 1). The mechanical properties of the welds, thus, show a strong direction of anisotropy. The same is true for the base material, if the mechanical strength in WD, respectively, TD is compared to the strength in ND [42].

Reasons for the differences in the mechanical properties observed in the base material and the welded joint can be attributed to hardening mechanisms, such as precipitation hardening, grain size or texture hardening.

Microscopy studies revealed precipitates in the fusion zone to be significantly coarser than in the base material, therefore, a significant effect of precipitation hardening on the mechanical strength of the fusion zone is not expected. Precipitation hardening by $Mg_{17}(Al,Zn)_{12}$ further cannot explain the strength anisotropy observed in the welded joints.

In the outer region of the fusion zone, the grain size is significantly smaller than in the base material and in the centre of the fusion zone. The high volume fraction of grain boundaries in the fusion zone contributes to its strengthening, but again does not account for the strong strength anisotropy observed.

Magnesium alloys due to their hcp structure are limited to only two independent easy slip systems $\{0001\}\{11-20\}$ basal slip and $\{10-12\}\{10-11\}$ pyramidal twinning [42,43] and the more complex slip on prismatic $\{10-10\}$ and pyramidal $\{10-11\}$ planes. A recent review of relevant literature revealed that basal slip has the lowest critical resolved shear stress (CRSS), ranging from 0.45–0.81 MPa, the CRSS of twinning is two to four times larger and prismatic slip has an even 48–87 times larger CRSS compared to basal slip [32]. In addition to dislocation slip, Mg typically deforms by mechanical twinning, in particular using the $\{10-12\}\{10-11\}$ system [35,42]. However, the amount of strain that can be accommodated by twinning is only about 6.5% [42]. Therefore, a strong influence of texture on deformation behavior of the welds can be expected.

The properties of the macroscopic samples in WD and TD represent the combination of the responses of the weld and the base material, whereas the properties of the micro flat tensile test specimens exclusively represent the intrinsic deformation behavior of the weld and the base material, respectively (Table 1). In the following, the evolution of texture during de-

formation of the welded joints in TD is discussed in detail using pole figures determined on the samples deformed to different maximum strains (Fig. 4; Table 1).

D_0 : In the fusion zone during in-plane tensile deformation along TD, the stress axis initially (point D_0 in Figs. 4, 10 and 12a) is perpendicular to the basal slip planes (0001). At a total strain of about 0.1% the stress–strain curve of the welded joints starts to be different from those of the base material and becomes non-linear indicating plastic deformation.

D_1 : The pole figure obtained in the fusion zone in point D_1 (Figs. 7 and 10a) clearly shows a reorientation of part of the basal poles into WD. This orientation is due to tensile twinning $\{10-12\}\{10-11\}$. The same twinning that changes the basal pole figure also changes the orientation of the prism planes $\{10-10\}$ and $\{11-20\}$. Almost no change in the texture of the base material shows that only basal dislocation slip may occur in the base material.

D_2 : At total strains between about 0.3% (D_1) and 0.6% (D_2) strain hardening in the fusion zone is very weak and the texture observed at point D_2 is not significantly different to the texture at point D_1 . Thus, the texture in point D_2 does not give evidence of the active deformation mechanism. The weak hardening observed presumably is due to basal slip in some favorably oriented grains. At the point D_2 the easy twin orientations have been exhausted and the material hardens because it is forced to a harder deformation mode. This is maybe due to an accumulation of cutting dislocations in the basal planes, which has frequently been suggested [44,45] as dominant hardening mechanism of Mg alloys. In addition $\{10-12\}$ twinning may substantially increase the hardening, because twin boundaries are intragranular obstacles for dislocation movement [46,47]. No texture change occurs in the base material.

D_3 : Pole figures obtained in the fusion zone of the sample where tensile deformation was stopped at point D_3 show a strong difference compared to the pole figures obtained at lower deformations. The basal pole of one fraction of the crystallites is in WD, the basal pole of the other fraction of crystallites is perpendicular to it (TD). The crystallographic orientation with basal poles in TD does not enable basal slip, thus favoring twinning and non-basal slip and, therefore, hardening becomes stronger. Due to tensile twinning the symmetry axis of the crystal lattice rotates 180° about the twin plane normal [15,44,48,49] resulting in a 86.6° reorientation of the basal pole from perpendicular to nearly parallel to the stress axis (Fig. 12b).

D_4 : By further increasing total strain the hardening again decreases and the pole figures obtained in the weld of the sample deformed to point D_4 show an almost complete reorientation of the crystallites with their basal poles into WD. The deformation mechanisms presumably are a combination of basal slip in favorably oriented grains whereas twinning and non-basal slip occur in those crystallites with their basal poles near TD (which then results in a reorientation of the basal poles in WD). At larger strains hardening decreases even stronger, thus, indicating basal slip in most crystallites. The

sample obtained at point D₄ gives evidence of strong plastic deformation of the weld compared to the sample deformed to point D₃ (Fig. 5).

D₅: Pole figures of the fusion zone obtained in point D₅ reveal most crystallites to be oriented with their basal poles in WD. The base material in the welded joint shows only a small change in texture when comparing pole figures obtained in point D₀ and point D₅.

The base material texture is a basal texture, typical for cold rolled AZ31B. In the fusion zone the basal planes are rotated about 80°, thus, their normal vectors almost lie in the sheet plane (Fig. 12a). Consequently, the differences in the mechanical behavior of the sheets and the weld can be explained by their distinct textures and the resulting differences in the deformation mechanisms activated (Fig. 12b).

5. Summary and conclusions

The microstructure–property relation of an Mg AZ31B laser beam weld was investigated. The results of microscopy, texture, residual stress analyses using synchrotron X-ray diffraction and mechanical tests reveal:

- Welds with high surface quality and low porosity were manufactured by a laser beam welding process without wire.
- The heat affected zone is very narrow, no grain coarsening was observed adjacent to the fusion line and microhardness values are almost uniform across base material HAZ and fusion zone.
- The residual stress distribution observed is typical for butt-joints and thermally induced welding residual stresses. Residual stress distributions at the top and at the bottom of the welds are very similar and the maximum tensile residual stress values measured were substantially lower than the yield stress of the base material and the fusion zone.
- The base material texture is a basal texture, typical for cold rolled AZ31B. In the fusion zone the basal planes are rotated about 80°, thus their normal vectors almost lie in the sheet plane. The growth of the crystallites in the direction of the heat flow causes a slight tilt of the *c*-axes of the crystallites out of the sheet plane.
- In tensile tests in transverse direction a lower yield strength of the welded joint compared to the base material is observed. This can be explained by the activation of different deformation mechanisms at different steps of tensile deformation. The dependence of the active deformation mechanisms on the total strain of the welds is apparent in pole figures determined within the weld and the adjacent parent material.
- Homogeneous deformation of weld and sheets would require a change in the welding process leading to different solidification conditions and, thus, a texture of the fusion zone similar to these of the base material.

Acknowledgements

This work was supported by the Contract RII3-CT-2004-506008 (IA-SFS) of the European Commission. HASYLAB

at DESY is acknowledged for beam-time at instrument G3 at DORIS. Dr. T. Wroblewski and Dr. A. Rothkirch, HASYLAB, are acknowledged for support during diffraction experiments using synchrotron radiation.

R.S.C. thanks the Program Alban – European Union Program of High Level Scholarships for Latin America – for financial support (scholarship NO. E04D046587BR). The Helmholtz society, within the framework of the virtual institute VI-PNAM, is also kindly acknowledged for financial support.

References

- [1] M.M. Avedesian, H. Baker, ASM Specialty Handbook: Magnesium and Magnesium Alloys, ASM International, 1999.
- [2] P.G. Sanders, J.S. Keske, K.H. Leong, G. Kornecki, J. Laser Appl. 11 (2) (1999) 96–103.
- [3] K.H. Leong, G. Kornecki, P.G. Sanders, J.S. Keske, ICALOE 98: Laser Materials Processing Conference, Orlando, FL, 16–19 November 1998, 1998, pp. 28–36.
- [4] X. Cao, M. Jahazi, J.P. Immarigeon, W. Wallace, J. Mater. Process. Technol. 171 (2006) 188–204.
- [5] L.K. Pan, C.C. Wang, Y.C. Hsiao, K.C. Ho, Optics Laser Technol. 37 (2004) 33–42.
- [6] L. Liming, W. Jiefeng, S. Gang, Mater. Sci. Eng. A 381 (2004) 129–133.
- [7] J.A. Esparza, W.C. Davis, E.A. Trillo, L.E. Murr, J. Mater. Sci. Letters 21 (2002) 917–920.
- [8] K. Behler, J. Berkmann, A. Ehrhardt, Mater. Des. 18 (1997) 261–267.
- [9] E. Schubert, M. Klassen, I. Zerner, J. Mater. Process. Technol. 115 (2001) 2–8.
- [10] W.F. Sheerly, R.R. Nash, Trans. Metall. Soc. AIME 218 (1960) 416.
- [11] T. Obara, H. Yoshinaga, S. Morozumi, Acta Metall. 21 (1973) 845.
- [12] H. Oshinaga, R. Horiuchi, Trans. JIM 5 (1963) 14.
- [13] J.F. Stohr, J.P. Porier, Philos. Mag. 25 (1972) 1313.
- [14] F.E. Hauser, P.R. Landon, J.E. Dorn, Trans. Am. Inst. Mining Metall. Eng. 206 (5) (1956) 589–593.
- [15] S.R. Agnew, C.N. Tomé, D.W. Brown, T.M. Holden, S.C. Vogel, Scripta Mater. 48 (2003) 1003–1008.
- [16] D.W. Brown, S.R. Agnew, M.A.M. Bourke, T.M. Holden, S.C. Vogel, C.N. Tomé, Mater. Sci. Eng. A 399 (2005) 1–12.
- [17] Z. Zuberova, Y. Estrin, T.T. Lamark, M. Janecek, R.J. Hellmig, M. Krieger, J. Mater. Process. Technol. 184 (2007) 294–299.
- [18] R. Zettler, A.C. Blanco, J.F. dos Santos, S. Marya, in: N.R. Neelamegham, H.I. Daplan, B.R. Powell (Eds.), Magnesium Technology, TMS, The Minerals, Metals & Materials Society, 2005.
- [19] J.C. Tan, M.J. Tan, Mater. Sci. Eng. A 339 (2003) 124.
- [20] H. Watanabe, H. Tsutsui, T. Mukai, M. Kohzu, S. Tanabe, K. Higashi, Int. J. Plast. 17 (2001) 387.
- [21] H. Watanabe, T. Mukai, M. Kohzu, S. Tanabe, K. Higashi, Acta Mater. 47 (1999) 3753.
- [22] W.J. Kim, S.W. Chung, C.S. Chung, D. Kum, Acta Mater. 49 (2001) 3337.
- [23] H. Somehawa, K. Hirai, H. Watanabe, Y. Takigawa, K. Higashi, Mater. Sci. Eng. A407 (2005) 53.
- [24] W. Woo, H. Choo, D.W. Brown, P.K. Liaw, Z. Feng, Scripta Mater. 54 (2006) 1859.
- [25] S.H.C. Park, Y.S. Sato, H. Kokawa, Scripta Mater. 49 (2003) 161.
- [26] S.H.C. Park, Y.S. Sato, H. Kokawa, Metall. Mater. Trans. A 34 (2003) 987.
- [27] W.B. Lee, J.W. Kim, Y.M. Yeon, S.B. Jung, Mater. Trans. 44 (2004) 917.
- [28] C.I. Chang, C.J. Lee, J.C. Huang, Scripta Mater. 51 (2004) 509.
- [29] M. Kocak, G. Cam, S. Riekehr, F. Torster, J. dos Santos, IIW-Doc. SC X-F-079-98, 1998.
- [30] S.F. Su, J.C. Huang, H.K. Lin, N.J. Ho, Metall. Mater. Trans. A 33A (2002) 1461–1473.
- [31] M.E. Fitzpatrick, A. Lodini, Taylor & Francis, London, 2003.
- [32] X.Y. Lou, M. Li, R.K. Boger, S.R. Agnew, R.H. Wagoner, Int. J. Plast. 23 (2007) 44–86.

- [33] S. Guldberg, N. Ryum, *Mater. Sci. Eng. A* 289 (2000) 143–150.
- [34] A. Styczynski, C. Hatig, J. Bohlen, D. Letzig, *Scripta Mater.* 50 (2004) 943.
- [35] C.S. Roberts, *Magnesium and Its Alloys*, Wiley, New York, 1964.
- [36] R.W. Cahn, *Acta Metall.* 1 (1953) 50–74.
- [37] V.A. Karkhin, V.V. Plochikhine, A.S. Ilyin, H.W. Bergmann, *Weld. World* 46 (2002) 11–12.
- [38] T.L. Teng, C.C. Lin, *Int. J. Pressure Ves. Pip.* 75 (1998) 857–864.
- [39] A.P. Mackwood, R.C. Crafer, *Opt. Laser Technol.* 37 (2005) 99–115.
- [40] T. Nitschke-Pagel, H. Wohlfahrt, *Mater. Sci. Forum* 404–407 (2002) 215–224.
- [41] H.K. Tönshoff, T. Friemuth, C. Podolsky, J. Winkler, H. Haferkamp, M. Niemeyer, V. Kaese, S. Janssen, *Mater. -wiss. U. Werkstofftech.* 32 (2001) 62–67.
- [42] S.R. Agnew, O. Duygulu, *Int. J. Plast.* 21 (2005) 1161–1193.
- [43] E.F. Emley, *Principles of Magnesium Technology*, Pergamon, Oxford, 1966.
- [44] M.M. Myshlyayev, H.J. McQueen, A. Mwembela, E. Konopleva, *Mater. Sci. Eng. A* 337 (2002) 121–133.
- [45] S. Tian, L. Wang, K. Sohn, K. Kim, Y. Xu, Z. Hu, *Mater. Sci. Eng. A* 415 (2006) 309.
- [46] M.R. Barnett, Z. Keshavarz, A.G. Beer, D. Atwell, *Acta Mater.* 52 (2004) 5093–5103.
- [47] S.R. Agnew, M.H. Yoo, C.N. Tome, *Acta Mater.* 49 (2001) 4227–4289.
- [48] M. Pastor, H. Zhao, T. DebRoy, *J. Laser Appl.* 12 (3) (2000) 91–100.
- [49] R.E. Reed-Hill, R. Abbaschian, *Physical and Metallurgy Principles*, 3 ed., PWS Publishing Company, Boston, MA, 1994, pp. 2116–4324.